Multi-physics approach to predict fatigue behavior of high strength aluminum alloy repaired via additive friction stir deposition

Palya, N. I.; Fraser, K. A.; Hong, Y.; Zhu, N.; Williams, M. B.; Doherty, K.; Allison, P. G.; Jordon, J. B.

Publisher's version / Version de l'éditeur:
https://doi.org/10.1007/s40192-023-00309-3
Integrating Materials and Manufacturing Innovation, 12, 4, pp. 441-455, 2023-11-01

NRC Publications Archive Record / Notice des Archives des publications du CNRC :
https://nrc-publications.canada.ca/eng/view/object/?id=ed0f2dc1-a022-4877-9ff9-6501e647a087
https://publications-cnrc.canada.ca/fra/voir/objet/?id=ed0f2dc1-a022-4877-9ff9-6501e647a087

Integrating Materials and Manufacturing Innovation (2023) 12:441–455
https://doi.org/10.1007/s40192-023-00309-3

TECHNICAL ARTICLE

Multi-physics Approach to Predict Fatigue Behavior of High Strength Aluminum Alloy Repaired via Additive Friction Stir Deposition

N. I. Palya[1,2] · K. A. Fraser[3] · Y. Hong[1,2] · N. Zhu[1,2] · M. B. Williams[1,2] · K. Doherty[4] · P. G. Allison[1,2] · J. B. Jordon[1,2]

Received: 25 July 2023 / Accepted: 31 August 2023 / Published online: 1 November 2023

Abstract

A smooth particle hydrodynamic (SPH) simulation of an additive friction stir deposition (AFSD) repair was used to inform a multi-physics approach to predict the fatigue life of a high strength aluminum alloy. The AFSD process is a solid-state layer-by-layer additive manufacturing approach in which a hollow tool containing feedstock is used to deposit material. While an understanding of the evolving microstructures is necessary to predict material performance, the elevated temperatures and strain rates associated with severe plastic deformation processes (SPDP) make accurate collection of experimental data within AFSD difficult. Without the ability to experimentally determine material history within the AFSD process, an SPH model was employed to predict the thermomechanical history. The SPH simulation of an AFSD repair was used to inform several microstructural models to predict material history during and after processing with AFSD and a post-processing heat treatment. These microstructure models are then used to inform a mechanistic microstructure and performance model to predict the fatigue life of an AFSD repair in AA7075.

Keywords Additive Friction Stir Deposition · Smooth Particle Hydrodynamics · Aluminum · Additive Manufacturing · Multi-Scale Modeling · Fatigue · Repair

Introduction

Additive friction stir deposition (AFSD) is a solid-state, friction-based, additive manufacturing process leveraging severe plastic deformation to deposit material layer-by-layer [1]. This is accomplished through feedstock material in the form of a solid bar, stacked strips, or machine chips being pushed through a hollow, rotating tool through which material is softened from the frictional and plastic heat generation at the tool face [2]. First, the hollow tool is rotated against the substrate such that sufficient heat is built up to deform the feedstock material, at which time the tool is raised to the desired layer height. Once at the desired layer height, an actuator force is applied to the feedstock filling in the gap between the tool and the substrate. Finally, the G-code containing the deposition path is executed, depositing material in the desired geometry. In general, solid-state processes operate below the melting temperature benefitting from solid-state microstructures by avoiding solidification effects [3]. This is significant for traditionally "non-weldable" alloys such as 6xxx and 7xxx series aluminums that are subject to hot cracking [4]. As AFSD results in material experiencing severe plastic deformation, significant grain refinement occurs within the deposited material as a result of dynamic recrystallization (DRX), providing a benefit from the Hall–Petch relationship [5]. Grains are refined during thermomechanical processing due to sufficient heating and dislocation pileup, resulting in large grains re-nucleating into multiple smaller grains with lower dislocation densities. These smaller grains contain a greater overall grain boundary (GB) area compared to their former state. The increased GB area acts as a barrier to dislocation movement, causing dislocations to repel each other as well as GBs, strengthening the material as the material resists the formation of new dislocations [6].

✉ J. B. Jordon
brian_jordon@baylor.edu

1 Point-of-Need Innovations (PONI) Center, Baylor University, Waco, TX 76704, USA

2 Department of Mechanical Engineering, Baylor University, Waco, TX 76704, USA

3 National Research Council Canada, Saguenay, QC, Canada

4 DEVCOM Army Research Laboratory, Aberdeen Proving Ground, Aberdeen, MD 21005, USA

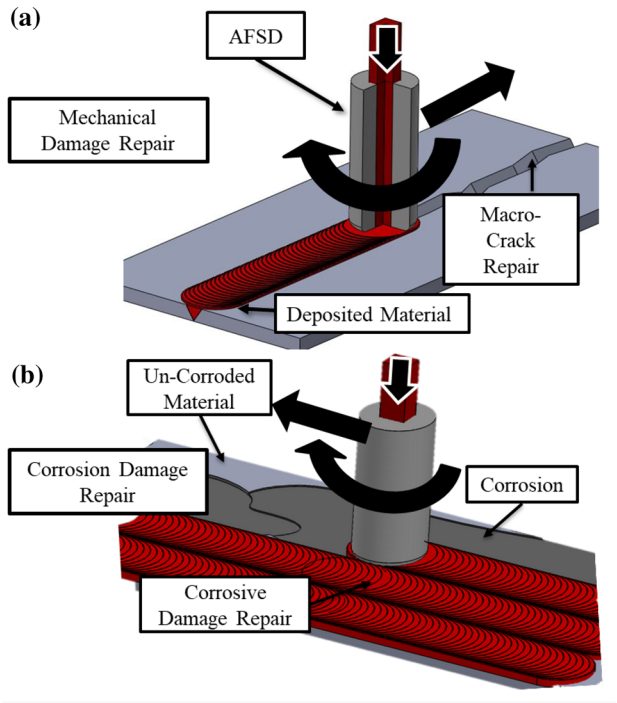

Fig. 1 **a** Schematic of an AFSD repair for crack repairs and **b** corrosion repairs

AFSD has shown to be a promising technology for repair applications due to the solid-state nature of the process. The use of filler material identical to the substrate reduces the electrical potential differences, minimizing the likelihood of galvanic corrosion [7]. Schematics of AFSD repair for corrosion and mechanical damage are shown in Fig. 1.

The nature of repair is significantly different from that of typical manufacturing, as its purpose is not to create a new component, but rather return an existing one to a functioning state [8]. To accomplish this, several considerations must be made, such as if original performance is acceptable, if different maintenance and inspection schedules are required, or if the repaired component will operate in an identical capacity to the original component [9]. In order to make these logistical decisions, an understanding and predictions of part performance must be obtainable. Ideally, this is accomplished through component repair, testing, and validation. While experimentation is critical to understating repair performance, a simulated approach to performance prediction can provide additional assessment tools that compliment non-destructive evaluation (NDE) and mechanical testing.

AFSD Process Modeling

Several approaches exist to simulate the thermomechanical history experienced during AFSD processing such as the finite volume method employed by Kincaid et al. [10]. Another option for process modeling of AFSD is a smooth particle hydrodynamics (SPH) approach. SPH is a collocation method in which the body being simulated is discretized into points representing small "elements" of the domain, similar to a finite element method (FEM). However, the SPH points, unlike the FEM elements, are individually non-deformable, are not tethered to a structured mesh, and are related through a smoothing function. Any deformation captured using the SPH method is seen through the movement of particles from their original geometry and an updated neighbor list, rather than deformation of individual elements. This allows for the SPH method to be well suited to simulating processes of significant plastic deformation such as AFSD and FSW, in which the initial and final geometries of the simulation greatly differ. The particle discretization method makes SPH well suited to particle tracking and capturing plastic strain and localized stress states [11]. FSW is one example of a severe plastic deformation process to employ SPH in a solid-state process model in work performed by Fraser et al. [12]. Other applications of SPH in solid mechanics include the modeling of the AFSD process by Stubblefield et al. for aluminum 6061 [11], friction stir extrusion [13], and cold spray [14] with the common theme between these works being they each required an approach capable of handling large deformations from the original geometry.

Microstructure Modeling

Due to the similar nature of the solid-state physics present in FSW, the AFSD process can be modeled with similar approaches, as they both experience similar temperature and strain rates resulting in DRX and grain refinement. Several microstructure evolution models are available, such as the Monte Carlo (MC) [15], cellular automaton (CA) [16], and phase field [17]. The phase-field method is a material thermodynamics-based approach based on Ginzburg–Landau theory [18], using differential equations to describe the effects of diffusion, ordering potential and thermodynamic driving force. The phase-field method has been widely applied to the calculation of DRX [19]. For this reason, when a thermomechanical history is provided, grain morphology can be predicted using phase-field simulations.

In a similar manner to grain morphology, precipitate evolution can be modeled from the SPH provided thermomechanical history to simulate the effects, temperature has on precipitate coarsening during processing. This can be accomplished using TC-PRISMA, the precipitate module of the commercially available software, Thermocalc Prisma [20]. Given temperature history, the resulting strengthening precipitate sizes and volume fractions can be determined using a thermodynamic and kinematics approach for a range of materials [21].

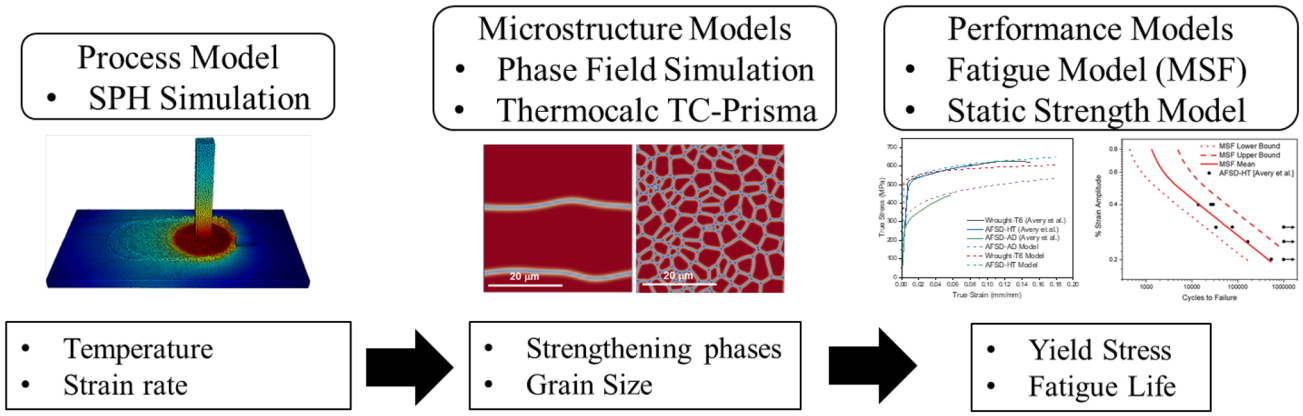

Fig. 2 Flowchart of MSF model population via simulated approach

Performance Modeling

A microstructure sensitive fatigue (MSF) model first proposed by McDowell et al. can be used to predict fatigue performance based on several material constants and the microstructure [22]. This model has been used to describe and predict the fatigue performance of several alloys of varied processing [23]. Additionally, the MSF model has been calibrated to AFSD processed AA7075 described elsewhere [24].

This present work aims to use experimental data sets as a point of comparison, and ultimately validation, of a fully simulation populated MSF model. Using the models and approaches described previously, the MSF model can be populated without the need for experimental inputs though an integrated computational framework of process modeling to microstructure to performance and fatigue life. This computational framework will allow for a fatigue prediction of AFSD repaired components through a simulated set of inputs, providing the opportunity to assess the viability of AFSD repairs prior to deposition. The computational framework from the SPH process model to MSF fatigue prediction is outlined in Fig. 2.

Methods

The framework proposed in this work involves the integration of several different models ranging from large-scale thermomechanical simulations of AFSD to microscopic phase-field simulations of DRX. A diagram of this computational framework illustrated in Fig. 2 shows the linkages of the process simulation to the fatigue performance predictions.

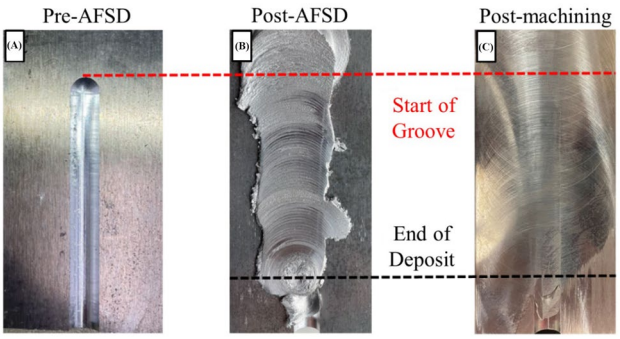

Fig. 3 AA7075 plate with simulated damage repaired via AFSD, (a) simulated damage prior to repair, (b) repaired plate after AFSD processing, (c) repaired plate after post process machining

AFSD Groove Repair

The process of an AFSD repair is shown in Fig. 3, in which an AA7075 wrought plate was machined by a ball nose end mill to simulate the process of repairing mechanical crack damage as shown in Fig. 1a. The AFSD process was used to deposit material into the groove, and then, the plate was machined flat, back to the OEM geometry.

SPH Method

To capture the complex physics occurring within AFSD processing, an SPH modeling approach was employed. In this present work, a research code, SPHriction-3D, was used to simulate the SPH process. This software allows for a hybrid approach, using both FEA and SPH components. Deformable bodies are modeled by SPH particles, the rigid, non-deformable bodies are modeled using FEM. The FEM parts include the anvil, the tool face, the actuator plate, and the sleeve for the feedstock. The FEM parts are shown in Fig. 4 as the transparent components, while the

SPH components can be seen in red and blue, representing the feedstock and substrate, respectively. The discretization used within this study is 1 mm, consistent with work by Stubblefield et al. in which the SPH approach is used to model the AFSD process [11].

The core of the SPH approach is the smoothing function that is the mechanism for constructing a continuum body from the individual SPH elements as a function of their nearest neighbors (Fig. 5). Several different smoothing functions have been applied for various SPH models, whereas the approach used in this present study is the hyperbolic spline function first used by Yang et al. [25] and employed by Stubblefield et al. [11].

$$W(R,h) = \propto_d \begin{cases} R^3 - 6R + 6 & \text{for } 0 \le R \le 1 \\ (2-R)^3 & \text{for } 1 \le R < 2 \\ 0 & \text{for } R \ge 2 \end{cases} \quad (1)$$

In order to model the non-uniform substrate for groove repairs, a biased SPH mesh was employed. This was done in order to maintain sufficient material points through every dimension of the substrate while being able to model the ball nose end mill groove geometry in this work. The biased SPH mesh is possible by weighting the influence SPH particles by not only their proximity to other particles as shown in Fig. 5, but also representative volume. By having different SPH particles represent different volumes, the modeling of the groove is possible without a smaller discretization that would be necessary if SPH particles were removed from the substrate to capture the intended geometry.

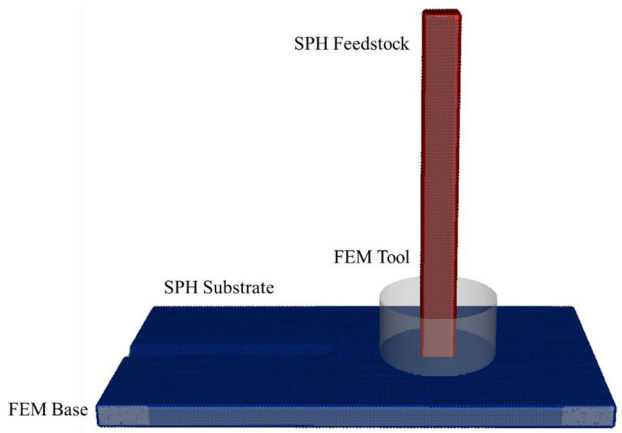

Fig. 4 SPH/FEM model set up of an AFSD repair using SPHriction-3D

SPH Formulations

The SPH model uses several continuum mechanics equations to capture the underlying physics of the interactions

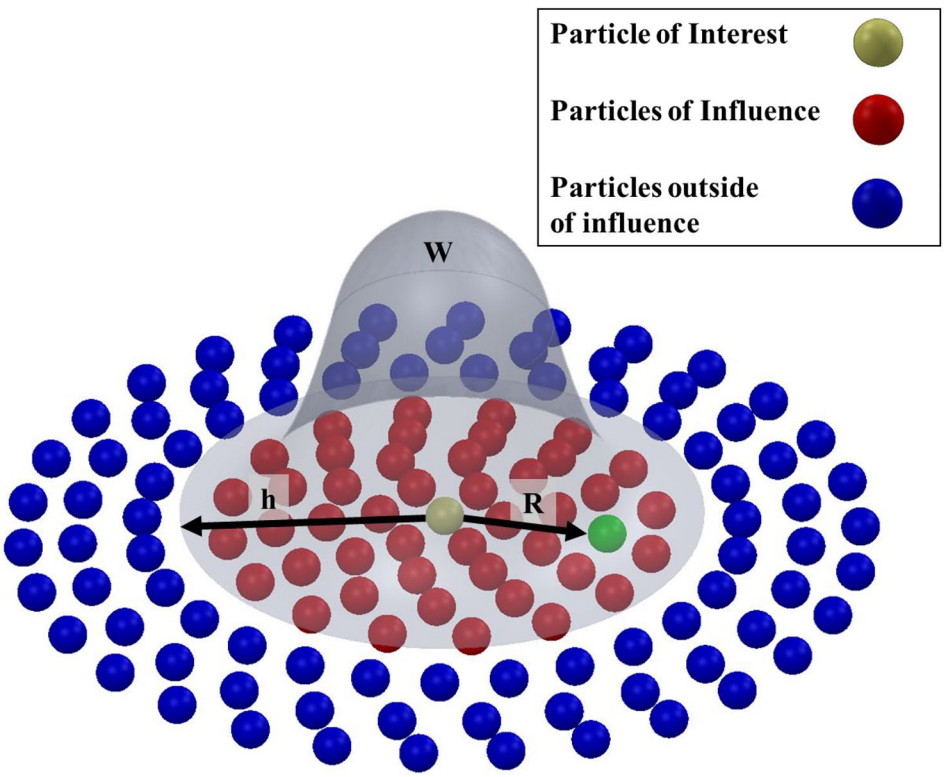

Fig. 5 SPH kernel function and the effect as a function of distance to a given neighboring particle

between each particle in the model. Due to the nature of each particle being influenced by its neighbors, SPHriction-3D is able to solve the underlying constitutive and continuum equations in parallel on graphical processing units, decreasing computational time compared to a serialized approach [26]. Each set of continuum mechanics equations is solved for each node as a function of its nearest neighbor over time within the simulation. The set of continuum equations solved in SPH are shown in Table 3 in the appendix. The nature of SPH allows for some advantages over other methods, namely, inherent particle tracking [27]. This allows for accurate strain prediction, and the ability to use the stress rate equation to calculate a history-dependent stress seen in Eq. (2) [11].

$$\dot{\bar{\bar{S}}} = 2G\left(\dot{\bar{\bar{\varepsilon}}} - \frac{1}{3}tr\left(\dot{\bar{\bar{\varepsilon}}}\right)\bar{\bar{\delta}}\right) + \bar{\bar{S}}\,\bar{\bar{\Omega}}^T + \bar{\bar{\Omega}}\,\bar{\bar{S}} \tag{2}$$

Using the SPH setup and formulations previously discussed, SPHriction-3D, is used to select a point within the repair geometry and to record the temperature and plastic strain history during deposition. The resulting output is the temperature and plastic strain experienced by that point in the model over the course of the repair. This history can then be passed to the subsequent models, specifically the phase-field and precipitate models. To ensure accurate temperature results would be passed off to the subsequent models, thermocouple validation experiments were conducted. The validation experiments were accomplished using a similar testing methodology to work done by Stubblefield et al. in which a steel backer plate with holes drilled in it was placed under the substrate, and k-type thermocouples attached to a Sper Scientific 800025 data logger were used to measure temperatures halfway through the substrate [11]. The SPH parameters used in this work were adapted from the literature [11] on AFSD simulations using an SPH method and are reported in the appendix.

Phase-Field Model

In this present work, a phase-field method in conjunction with a Kocks–Mecking (KM) dislocation model was used to analyze DRX and grain growth in a AA7075 during AFSD processing according to the method proposed by Takaki et al. [28]. The KM model allows for prediction of the average dislocation density resulting from the significant strain rates, and ultimately DRX, experienced during AFSD processing. The thermomechanical history in the form of temperature and strain rate needed for input is generated from SPH simulation results of the AFSD process. This thermomechanical history can then be used to model the behavior of the grain structure throughout AFSD processing of varying parameters. The high temperatures and strain rates recrystallize grains present in the feedstock material as it is deposited under the tool. When subjected to high temperatures and severe plastic deformation, dislocations are introduced. Subsequently during deposition, the DRX process results in these dislocations being eliminated though the nucleation of new grains. The energy of these dislocations drives recrystallized grain growth [29].

According to the KM model [30], the dislocation pileup resulting from plastic deformation, which in our case is due to the AFSD process, can be written as follows:

$$\frac{\mathrm{d}\rho}{\mathrm{d}\varepsilon} = k_1\sqrt{\rho} - k_2\rho \tag{3}$$

where ε is the true strain, and k_1 and k_2 are the hardening and softening coefficients, respectively. In order to derive Eq. (7), true stress σ must first must be related to the dislocation density ρ though the following equation proposed by Bailey-Hirsch [31].

$$\sigma = \alpha G b\sqrt{\rho} \tag{4}$$

Once true stress is related to dislocation density in Eq. (4), Eqs. (3) and (4) can be combined into the following form:

$$\frac{\mathrm{d}\sigma}{\mathrm{d}\varepsilon} = \frac{1}{2}\alpha G b k_1\left(1 - \frac{1}{\alpha G b}\frac{k_2}{k_1}\right) \tag{5}$$

k_1 and k_2 can be expressed as follows:

$$k_1 = \frac{2}{\sigma_{\mathrm{st}}}\frac{\mathrm{d}\sigma}{\mathrm{d}\varepsilon}\bigg|_{\sigma=0} \qquad k_2 = \frac{\alpha G b k_1}{\sigma_{\mathrm{st}}} \tag{6}$$

where α is the fitting coefficient, G is the shear modulus, and b is the Burgers vector. σ_{st} is the steady-state stress and can be calculated as follows:

$$\sigma_{\mathrm{st}} = \left[A_1\dot{\varepsilon}\exp\left(\frac{Q_{\mathrm{a}}}{RT}\right)\right]^{\frac{1}{A_2}} \tag{7}$$

Q_{a} is the deformation activation energy, R is the gas constant, and $\dot{\varepsilon}$ and T are the input parameters according to SPH calculation results. A_1 and A_2 are fitting constants.

For each grain in the phase-field model, a new variable, ϕ_i, is used. i being the index for each field for every ith grain,

$\phi_i = 1$, inside the grain i,

$\phi_j = 0$, $(j \neq i)$, outside the grain i,

$0 < \phi_i < 1$, at the interface.

According to the DRX model proposed by Takaki et al. [28], the time evolution of ϕ_i is expressed by solving:

$$\frac{\partial \phi_i}{\partial t} = \sum_{j=1}^{n} \frac{2M_{ij}^{\phi}}{n} \left[\sum_{k=1}^{n} \left\{ \left(W_{ik} - W_{jk} \right) \phi_k + \frac{1}{2} \left(a_{ik}^2 - a_{jk}^2 \right) \nabla^2 \phi_k \right\} - \frac{8}{\pi} \sqrt{\phi_i \phi_j} \Delta f_{ij} \right] \tag{8}$$

where M_{ij}^{ϕ} is the phase-field mobility,W_{ij} is the energy barrier, a_{ij} is the gradient energy coefficient, and f_{ij} is the stored energy difference of the GB between any given grains. The change in this energy difference,f_{ij}, can be solved as follows:

$$\Delta f_{ij} = \frac{1}{2} G b^2 \left(\rho_i - \rho_j \right) \tag{9}$$

During recrystallization, the deformation of the GB is the main nucleation mechanism as grains are deformed, as is the case during AFSD processing [32]. In order for this deformation of the GB to occur, a critical dislocation density, ρ_c, is required. This critical dislocation density for GB deformation can be expressed as follows [33]:

$$\rho_c = \left(\frac{20 \gamma \dot{\varepsilon}}{3 b l M \tau^2} \right)^{\frac{1}{3}} \tag{10}$$

where γ is the GB energy, M is the GB mobility, and l is the dislocation mean free path. Within this work, a uniform dislocation density within each grain is assumed. The model parameters of the phase-field simulations conducted in this work are reported in appendix.

Strength Model

AA7075 derives its strength from several strengthening mechanisms. To determine the final strength of material processed through AFSD without mechanical testing, the following strengthening mechanisms are considered.

Precipitates

In 7xxx series alloys, precipitates act as the dominate barrier to dislocation movement in the peak age condition, balancing precipitate cutting with Orowan looping behaviors for small and large precipitate sizes, respectively [34, 35]. For AA7075 in the T6 state, this precipitate is the meta-stable η' phase [36]. The strength contribution from these precipitates is described by the following relationships [37]:

$$\Delta \tau_{\text{Rods}} = \frac{A}{\delta \sqrt{3} \left(\sqrt{\frac{\pi}{6f}} - \sqrt{\frac{2}{3}} \right)} \ln \left(\frac{\sqrt{2} \delta}{r_o} \right) \tag{11}$$

$$A = \frac{0.85 G b}{2\pi (1 - v)^{\frac{1}{2}}} \tag{12}$$

where r_o is the dislocation core radius, f is the volume fraction of the precipitate, and δ is the diameter of the precipitate. The precipitate evolution during processing is integral to the resulting properties of the AFSD repair. The evolution and coarsening of precipitates that occur during AFSD processing is modeled using the software Thermocalc Prisma and associated databases. The details of the approach employed by Thermocalc can be seen elsewhere [20].

Grain Boundary

Grain boundaries can provide contributions to material strength by acting as barriers to dislocation movement. This can be described by the Hall–Petch relationship in which smaller grains result in higher strength materials. This is due to the decreased area in smaller grains being incapable of accommodating as many dislocations as their larger counterparts. This relationship can be expressed in the form [38]:

$$\sigma_{gb} = \sigma_f + k_i d^{-m} \tag{13}$$

where σ_f is the yield strength of pure aluminum, k_i is the Hall–Petch constant of 0.065 MPa $m^{-\frac{1}{2}}$ [39], d is the average grain size, and m is GB strengthening exponent of 0.5.

Solid Solution

Alloying elements dissolved within the bulk matrix are another significant source of strength of aluminum alloys. This is due to differences in atomic size of the various alloying elements resulting in a misfit within the aluminum matrix. These elements can be substitutions in which they replace an aluminum atom within the matrix resulting in distortion of the matrix if the element is larger or smaller than the aluminum atom if it is replacing or can be interstitial if it exists in between the lattice structures. Interstitial atoms fit between atoms in the matrix, distorting the matrix and once again acting as barriers to dislocation movement through the lattice. The strength of these alloying elements contribute is dependent on their size and concentration described for each element by the equation [40]:

$$\Delta \tau_{\text{ss}} = A {C_o}^{2/3} \tag{14}$$

where A is the element constant, and C_o is the element concentration in solution. The average of AA7075 element concentrations was used in this work to calculate strength in the T6 state seen in Table 1 along with the values of the element constants [38].

The total solid solution strengthening of the alloy is a linear combination:

Table 1 7075 composition and constants used for solid solution strengthening

Element	A	Conc.
Cu	12.431	1.6
Mn	15.772	1.5
Mg	20.431	2.5
Zn	3.085	5.6

$$\Delta\tau_{ss} = \Delta\tau_{Cu} + \Delta\tau_{Mg} + \Delta\tau_{Mn} + \Delta\tau_{Zn} \tag{15}$$

Stacking Fault

A secondary phenomenon relating to the precipitates within AA7075 is stacking fault strengthening. As the stacking fault energies of the bulk matrix and the precipitates are not equal, the movement of partial dislocations is impacted depending on the phases present in their path [41]. This can be accounted for using the equation [42]:

$$\Delta\tau_{sf} = \left(\frac{Kf}{\gamma_{sf}}\right)^{\frac{1}{2}}\left(\frac{\Delta\gamma}{b}\right)r_p^{-\frac{1}{2}} \tag{16}$$

$$K = \frac{Gb_p^2}{8\pi(1-\nu)}\left(2-3\nu+4\nu\sin^2\frac{\pi}{2}\right) \tag{17}$$

where b_p is the Burgers vector for the partial edge dislocation along the <1 1 2> plane in aluminum [38].

$$\gamma_{sf} = \frac{\gamma_{sfm} - \gamma_{sfp}}{2} \tag{18}$$

where γ_{sfm} is the stacking fault energy of aluminum $= 200\ \mathrm{mJ/m^2}$ [43], and γ_{sfp} is the stacking fault energy of the η' phase $= 600\ \mathrm{mJ/m^2}$ [44]. $\Delta\gamma$ is the absolute value of the difference between stacking fault energy of aluminum and the η' phase.

Dislocation

To capture the impacts of strain hardening within the AFSD process, a method that incorporates dislocation density is employed. This is due to the occurrence of DRX during the AFSD process. The assumption of constant dislocation density before and after processing cannot be made. Due to this fluctuation in dislocation density, the strain hardening equation:

$$\tau = \alpha G b \rho^{\frac{1}{2}} \tag{19}$$

is used [45]. The dislocation density, ρ, allows for the reduction of dislocations after DRX to be accounted for in the analysis. This approach prevents an over prediction of the dislocation contribution to the strength of the AFSD-T6 material condition by accounting for dislocation losses from DRX.

MSF Modeling

In order to model the fatigue behavior of material processed through AFSD, the microstructure sensitive fatigue (MSF) model is employed to relate the microstructure and mechanical property predications to component performance and fatigue life. This is accomplished through modeling the different experimentally observed stages of fatigue damage including, crack incubation, microstructurally small crack growth, physically small crack growth, and long crack growth. This approach can be summarized equation used to obtain the total cycles to failure [24]:

$$N_{total} = N_{inc} + N_{\frac{MSC}{PSC}} + N_{LC} \tag{20}$$

Equation (20) consists of the number of cycles for incubation, small crack growth, and long crack growth denoted by N_{inc}, $N_{\frac{MSC}{PSC}}$, and N_{LC}, respectively. The incubation life contribution, N_{inc}, is assumed to be composed of two main phases, microcrack nucleation followed by the early stages of microcrack propagation through the tip of the microscopic notch. Microstructurally/physically small crack growth, $N_{\frac{MSC}{PSC}}$, is the contribution to total cycles consisting of crack growth from the early stages at which it would be considered microstructurally small to the upper limit of this range when it is classified as a physically small crack. The final stage of crack growth is long crack propagation, N_{LC}, consisting of the number of cycles required to go from a long crack to failure of the material. A calibrated MSF model for AA7075 and the corresponding coefficients are reported elsewhere [24, 46].

Results and Discussion

Results from the advance phase of the AFSD in which the tool is moving in the traverse direction of this simulation are shown in Fig. 6. The advance phase of the AFSD was of particular interest in the validation study as this is the period of processing where the most extreme temperatures are experienced within the deposition. Any coarsening of strengthening phases is most likely to occur during these peak temperatures. The advance phase of processing is the most repeatable period of AFSD processing and was used for temperature validation.

Figure 6 shows the SPH simulation and the experimental validation of temperatures for AFSD deposits conducted at the same parameters as prior work by Avery et al. [46]. The experimental thermocouple results show a significant difference in the advancing and retreating

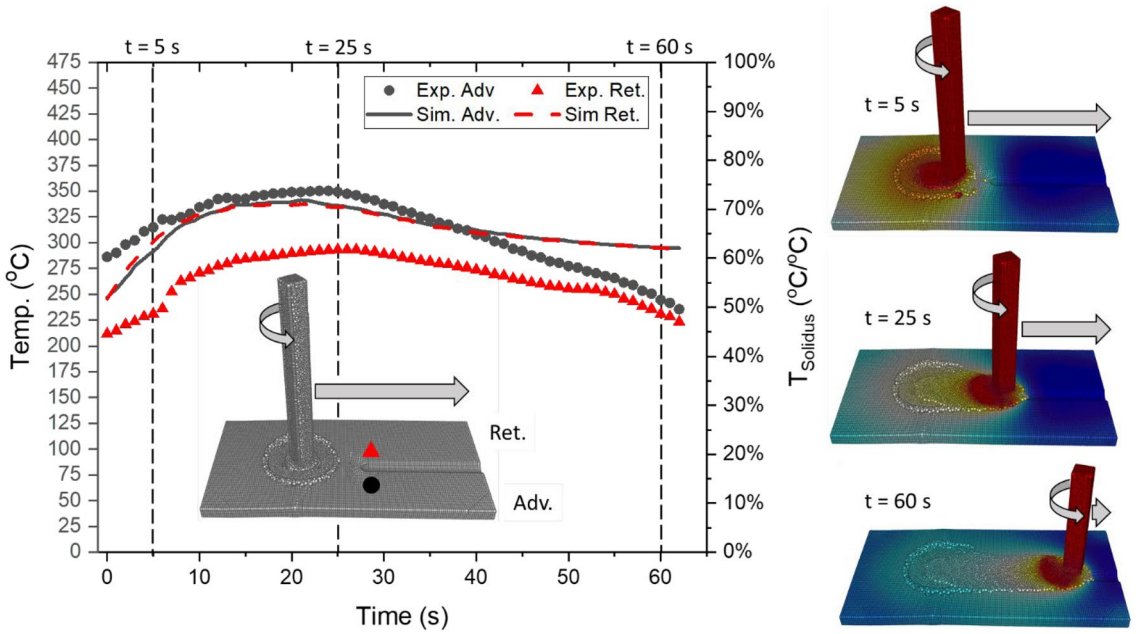

Fig. 6 SPH temperature predictions compared to thermocouple measurements taken from the advancing and retreating side of the tool

sides, consistent with work by Stubblefield et al. [11]. The temperature differences are the most pronounced at the beginning of the advance phase when the tool is closest to the thermocouple location with a reduced effect as the tool moves away from the measurement location toward the end of the deposition. Peak temperatures of 350 °C and 293 °C were seen in the advancing side and retreating side of the tool, respectively, by the thermocouples. SPH simulation results showed significantly less temperature differences on the advancing and retreating sides of the tool reaching 341 °C and 337 °C. The differences in the temperatures seen on either side of the tool were far less pronounced in the SPH simulation seeing on average only 3 °C of difference opposed to the 57 °C recorded by the thermocouple data. Some of this difference in tool temperature bias can be explained by back extrusion into the thermocouple backing plate on the advancing side. This was present on all three of the thermocouple validation experiments due to material having a preference to deposit on the advancing side of the tool. For this reason, a location on the advancing side of the tool was used to provide the thermomechanical history to the subsequent models as the advancing side temperatures showed greater alignment with the experimental data.

Phase-Field Grain Size Outputs

The first step in populating the strength model and subsequently the MSF model is to use the SPH thermomechanical history to predict the resulting grain size after processing. The temperature history and plastic strains predicted by the SPH model were passed to a phase-field model. The boundary conditions of the phase-field simulation were provided by the SPH outputs, where these results are shown in Fig. 7.

Figure 7 shows the comparison of the predicted microstructure before and after AFSD processing. The long, columnar grains are shown in Fig. 7a and b resulting from the cold rolling process. This feedstock microstructure was used as the pre-AFSD condition based on EBSD scan results from the wrought AA7075 from Avery et al. [46]. After AFSD processing, experimental data shows evidence of DRX and grain refinement in both the experimental EBSD scan in Fig. 7c and the phase-field model in Fig. 7d. The phase-field model predicted an average grain size of 4.23 µm. This is within the range of grain sizes measured in experimental work in Fig. 7c and throughout the repair ranging from 3.5 to 6 µm [46]. The phase-field simulations also predicted a similar equiaxed structure in the as-deposited AFSD material that was observed experimentally. The other critical output from the phase-field model is the dislocation density. This output is then able to be used to predict the strength contribution from work hardening and subsequent strength loss from DRX where dislocation dense grains nucleate into smaller less dislocation dense grains. The dislocation density of AFSD processed grains after undergoing dynamic recrystallization predicted by the phase-field model was 7.78×10^{12} m^{-2}. This is a significant reduction from the T651 cold rolled material of 3.28×10^{14} m^{-2} in the pre-AFSD feedstock material [47].

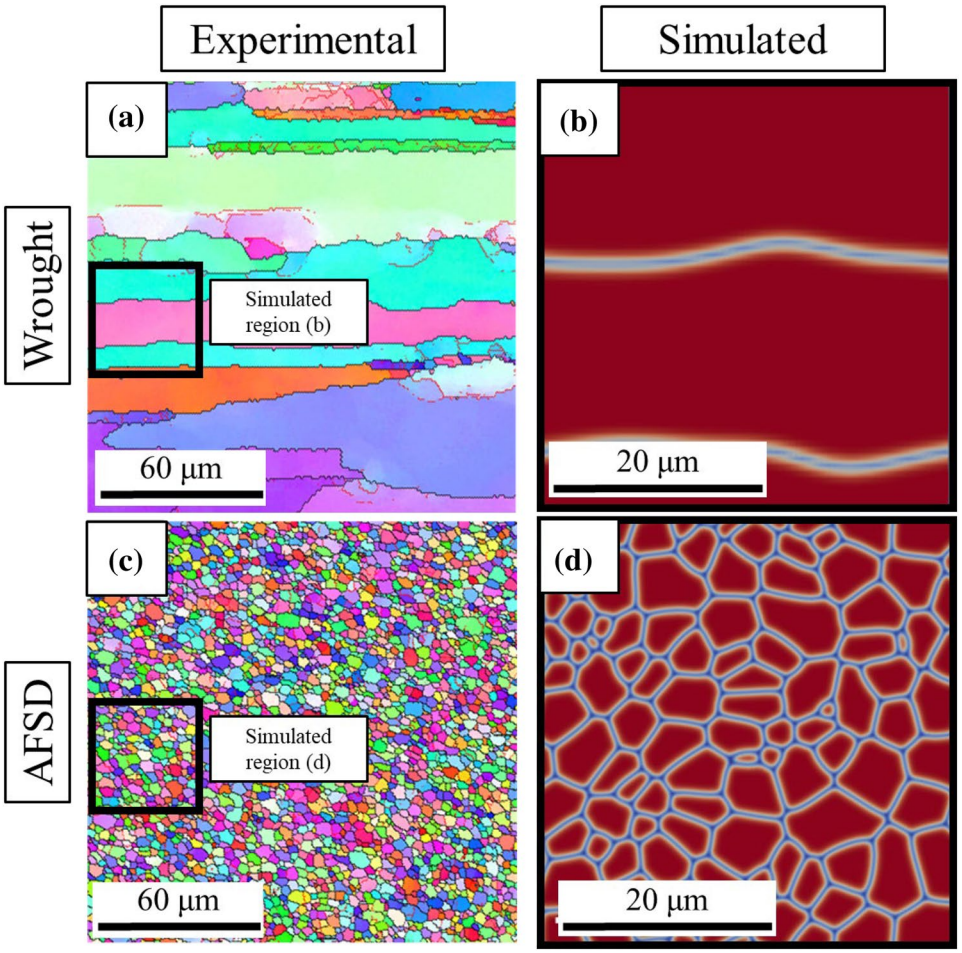

Fig. 7 **a** EBSD scan of AA7075 rolled plate (modified from [46]) and **b** the phase-field simulation of grain size before AFSD processing compared **c** EBSD scan of AA7075 after AFSD repair (modified from [46]) and **d** phase-field simulation of grain size after AFSD processing

Thermocalc Precipitate Size Outputs

The same thermal history used for the phase-field simulations was also used for the precipitate evolution model in Thermocalc TC-Prisma. The volume fraction and radius of the dominant strengthening phase, η', was simulated with the T6 peak age state as the starting point. This model considered only the η' and η phases as it related to the T6 condition. Based on the literature, there exists the possibility for other phases such as the T phase or S phase at these temperatures [36]. These phases were excluded from the results shown in Fig. 8, as the η' precipitate is considered to be the primary strengthening phase in 7075 [48].

Figure 8a shows the volume fraction of η' against the temperature conditions, the material is subjected to during AFSD processing at parameters of 25.4 mm/min for both the feedrate and the traverse rate with a tool rotation of 225 RPM. The AFSD processing temperature profile, shown in red, begins in which material temperatures steadily rise during the dwell phase of the AFSD process. The rate of temperature increase reduces during the time, the tool is raised off the substrate to the desired layer height and then begins to rapidly increase during the fill stage of the process in which deposited material is filling the gap between the tool and substrate. At these stages of processing, the volume fraction of η', shown in blue, slowly decreases with minimal overall change as the temperature rises from 20 to 200 °C. It is at the end of this fill phase when the η' volume fraction drastically decreases around 220 °C. This drop in the volume fraction of η' corresponds to an increase in the volume fraction of η shown in black. The η' precipitates are not reentering solution but rather coarsening to the η phase, which contributes significantly less to the strength of the material. With AA7075 being primarily a precipitate strengthened alloy, high heat input seen in both the SPH and thermocouple data, coupled with decreased strength in mechanical performance would be consistent with the loss of primary strengthening precipitates. As will be further discussed in later sections, this reduction in the η' phase is the most significant contribution to the lower yield of as-deposited AA7075 material properties. This is consistent with the comparison of yield strengths for peak age AA7075-T6 before and after being processed though FSW [49].

Figure 8b shows the same thermal history seen in Fig. 8a, but plotted against the mean radius of the η and η'

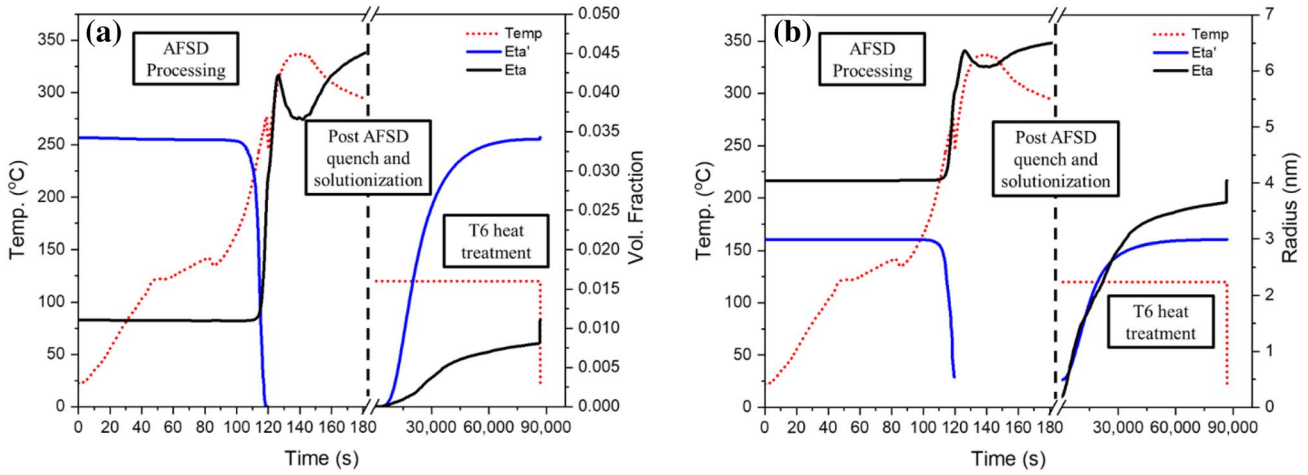

Fig. 8 η and η' (**a**) volume fraction and (**b**) radius as a result of temperatures experienced during AFSD processing and heat treatment

phases. Minimal changes in the radius for both phases are seen until 220 °C where the η phase significantly coarsens to roughly 6 nm. This coarsening corresponds with an increase in the volume fraction of the η phase in Fig. 8a. The simulation also predicts a drastic reduction in the mean radius of the η' phase as it approaches a volume fraction of zero. The significant reduction in radius of the η' phase suggests that the working temperature is above the solvus line for η'. The reduction in radius and volume fraction of η' corresponded with increases in both radius and volume fraction of the η phase. From the literature, it is expected to see the formation of T phase at these temperatures [36]. The lack of T phase in the precipitate model likely accounts for the over prediction of η phase volume fraction seen in Fig. 8a. The significant coarsening of the precipitates will result in an overall lower strength for the as-deposited material. As precipitates coarsen, they no longer provide a benefit in terms of strength to the alloy from the competing mechanisms of cutting and looping as they did in the peak age state. Larger precipitates begin to shift into the Orowan looping regime as particles become too large to be cut by dislocations. This results in only a single mechanism dominating precipitate strengthening as opposed to the competing mechanisms at smaller sizes that produce the characteristic high strength of peak age alloys. The further implications of coarsened precipitates will be discussed further in the next section as it relates to yield strength prediction of as-deposited and AFSD-T6 repairs.

The rapid decrease in the volume fraction of the η' phase at 220 °C in Fig. 8a suggests that for single-layer AFSD repairs such as those studied within this present work, a reduction in working temperature would result in significant strength increases in as-deposited material properties. This can be seen in the relationships presented in Eqs. (11) and (12), as smaller less coarsened precipitates will result in higher strengths. Future work should focus on minimizing the working temperature of AFSD depositions of precipitate hardened alloys.

After the quench and solutionization denoted by the break in Fig. 8, the T6 heat treatment returns the precipitates back to the pre-AFSD, T6 condition in both volume fraction and radius as seen after the break in Fig. 8.

AFSD Strength Prediction

Figure 9 shows the various distributions of strengthening mechanisms present for AA7075 for different processing conditions experienced by the material. The numerical contributions to each of these predictions are shown in Table 2. The AA7075-T6 distribution shows precipitate strengthen as the dominant mechanisms followed by stacking fault strengthening, which also relies on the size and volume fraction of the η' phase. Both of these are classified as precipitates in Fig. 9 as discussed in "Stacking Fault" section. The next three largest contributions come from dislocation strengthening, solid solution, and finally GB strengthening. For the AA7075-T6 state, the contribution to strength from dislocations depends on the dislocation density. Data provided in the table were obtained for rolled plate using values from the literature [47]. The AFSD as-deposited AA7075 material condition shows significant reduction in strength compared to the peak age condition. The strength contributions are distributed differently than the peak age with a reduced contribution from every mechanism. The reduced solid solution and precipitate strengthening resulted from the coarsening of the η' phase to η. The loss of the stacking fault strengthening is assumed to be a result of the incoherent nature of the η phase and the lack of dislocation density from DRX both of which are factors in the formation of stacking faults in high stacking fault energy materials [41]. The final material condition, AFSD-T6, appears similar to that of the T6 wrought condition

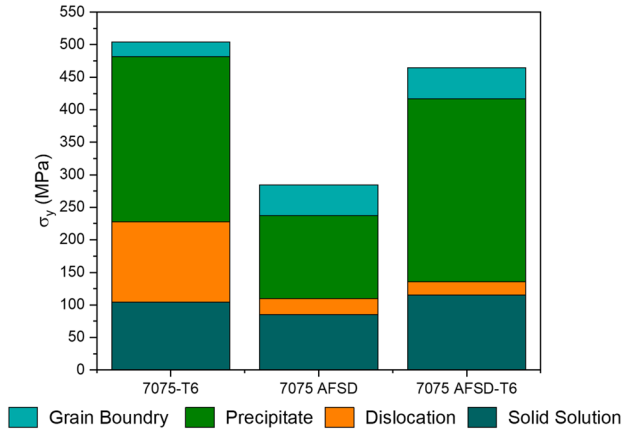

Fig. 9 Predicted strengthening mechanism contribution for AA7075, T6, AFSD as-deposited, and AFSD-T6

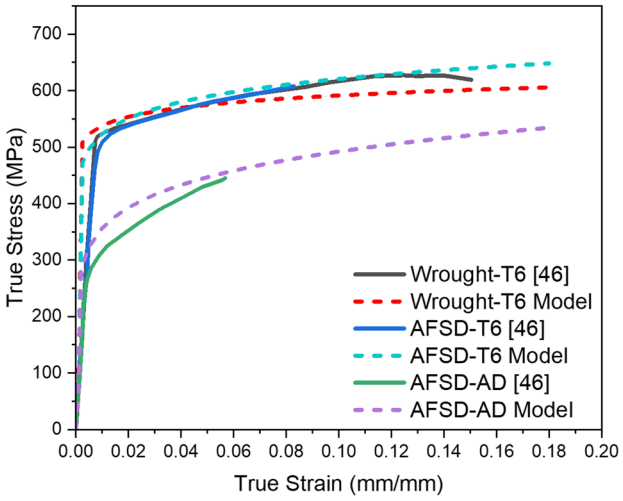

Fig. 10 Simulated tensile performance of AA7075-T6, AA7075 as-deposited, and AA7075-AFSD-T6

with the exception of an increased contribution from the refined grain structure left by AFSD and significant loss of dislocation strengthening from the DRX process.

Ductility and Ultimate Tensile Strength

A reduction in ductility can be presented for material repaired through AFSD. This trend is captured within the MSF model. The scatter in ductility of AFSD-T6 repairs (2–9%) adds complications to the prediction of ultimate strength [46]. Ultimate strength is a required input for the MSF model. In order to capture the conservative scenario for any given AFSD repair, a 2% strain to failure was used. This is shown in Fig. 10 depicting the simulated tensile performance of AA7075-T6, AA7075 AFSD as-deposited, and AA7075-AFSD-T6 compared to the experimental for all three material conditions from Avery et al. [46]. The static strength models in Fig. 10 "fracture" at a 2% strain to failure, where this failure strain is used to represent the UTS for each curve within the MSF model.

Combined Results and Final MSF Outputs

The final model in the framework proposed in this present work is the MSF fatigue prediction model. The MSF material constants used within this model can be seen in prior work on AFSD processed AA7075 by Avery et al. [46]. To this point, simulations in this work model the thermomechanical processing during AFSD and its macroscopic impacts on the material. These macroscopic effects are then used to relate processing conditions to resulting microstructure and finally mechanical properties in the form of material strength. A calibrated MSF model is used to account for effects otherwise unaccounted for in the other microstructure models proposed in this work such as iron-rich intermetallic particle size. The results from the fully simulated MSF model are shown in Fig. 11 along with experimental data from Avery et al. [46].

Figure 11a shows the upper and lower bounds of predicted cycles to failure generated using the framework proposed in this work for an AFSD repair that was subjected to a T6 post-processing heat treatment. The lower bound was generating using a grain size and intermetallic particle size of 12 µm and 7 µm, respectively. The upper bound was generating using a grain size and intermetallic particle size of 1.5 µm and 0.4 µm, respectively. These intermetallic sizes were determined though a relationship between deposition pitch and intermetallic grain refinement given as follows:

$$R_{\%} = 0.0364\, D_{IM}^{2} + 0.039\, D_{IM} \tag{21}$$

where $R_{\%}$ is the percent refinement of iron-rich intermetallic, and D_{IM} is the diameter of the iron-rich intermetallic. The mean MSF prediction captures the overall fatigue behavior

Table 2 Predicted strengthening mechanism contribution for AA7075, T6, AFSD as-deposited, and AFSD-T6 (all units are in MPa)

	SS	*D*	Rods	SF	GB	Pred. total	Experimental
T651	104.3	123.3	146.2	107.9	22.5	504	503
AFSD	85.2	24.2	127.3	0	47.6	284	285
AFSD-T6	115.3	20.6	161.6	119.3	47.6	464	490

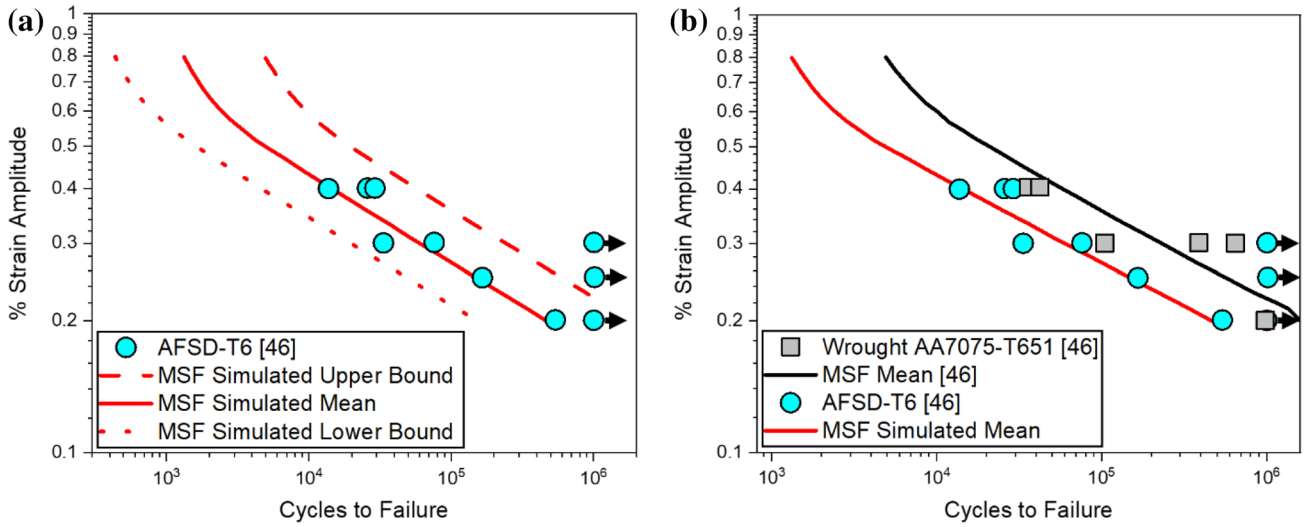

Fig. 11 **a** Fully simulated MSF predictions of fatigue life performance of AFSD-T6 compared to experimental data [46] and **b** mean MSF for wrought AA7075-T651 from Avery et al. compared to MSF simulated mean

seen in the experimental work from Avery et al. [46]. The upper and lower bounds of the predictions follow the trend of a smaller grain size and intermetallic particles, resulting in greater cycles to failure. Figure 11b shows the comparison of the AFSD-T6 fatigue performance compared to the wrought experimental fatigue data and MSF predictions from Avery et al. [46].

Advantages and Disadvantages of this Approach

The approach proposed in this present work allows for predictions of mechanical performance of material processed through AFSD, where these predictions require SPH thermomechanical simulations, phase-field simulations, and a calibrated MSF model. The development of these models and simulations generally follows significant mechanical testing and understanding of mechanisms within a given manufacturing process. While this framework is general enough to apply to a range of manufacturing methods outside of the AFSD repair case presented here, the understanding and mechanical testing required for such expansions of this framework are not insignificant. Many of the inputs used in this work relied on published data; however, this may not be available for every manufacturing process that one may wish to expand this numerical approach to, and additional mechanical testing may be required. However, once that testing has been done to properly populate the necessary inputs, this approach can allow for further understanding of these relationships across a wide range of complex geometries and boundary conditions that would otherwise be burdensome to test individually. In addition, if this approach was used to determine the differences in material properties within a repaired component as part of a larger simulation (e.g., FEM), the latter half of this approach would need to be repeated several times to capture all of the strain rate and temperature gradients present within an AFSD repair.

Conclusion

In this present work, a multi-physics model framework to predict AFSD repair performance was presented. An SPH process model of AFSD was used to generate a thermomechanical history experienced during processing. The thermomechanical history is then used in microstructure models to provide grain size, precipitate size, and dislocation density. These outputs are then used to predict the strength of as-deposited and post-process heat-treated AFSD repairs through a combination of strengthening mechanism contributions. Finally, these outputs populate the MSF fatigue model in order to provide a fatigue life performance of AFSD repairs. The predicted yield strength of both as-deposited and post-process heat-treated samples saw good agreement to experimental values in prior work. The mean and bounds of the MSF predictions saw good agreement with experimental work performed by Avery et al. for AFSD repairs processed under the same processing parameters [46]. The upper and lower bounds of the MSF prediction were able to capture the scatter of experimental results of AFSD repairs of AA7075. The approach proposed in this work was applied for a single location within the AFSD repair. A similar methodology can be applied and used to populate further models such as a finite element approach to further simulate the resulting fatigue crack propagation as informed by the MSF populated using the methodology proposed in this work.

Appendix

See appendix Tables 3, 4, 5, and 6.

Table 3 SPH formulations of continuum equations

Equation	SPH formulation
Strain rate	$\dot{\varepsilon}_i^{\alpha\beta} = \frac{1}{2}\sum_{j=1}^{N_i}\left(\frac{m_j}{\rho_j} v_{ji}{}^{\alpha}\frac{\partial W_{ij}}{\partial x_i{}^{\beta}} + \frac{m_j}{\rho_j} v_{ji}{}^{\beta}\frac{\partial W_{ij}}{\partial x_i{}^{\alpha}}\right)$
Spin tensor	$\Omega_i^{\alpha\beta} = \frac{1}{2}\sum_{j=1}^{N_i}\left(\frac{m_j}{\rho_j} v_{ji}{}^{\alpha}\frac{\partial W_{ij}}{\partial x_i{}^{\beta}} - \frac{m_j}{\rho_j} v_{ji}{}^{\beta}\frac{\partial W_{ij}}{\partial x_i{}^{\alpha}}\right)$
Jaumann stress rate	$\frac{dS^{\alpha\beta}}{dt} = 2G\left(\dot{\varepsilon}^{\alpha\beta} - \frac{1}{3}\delta^{\alpha\beta}\dot{\varepsilon}^{\gamma\gamma}\right) + S^{\alpha\gamma}\Omega^{\beta\gamma} + \Omega^{\alpha\gamma}S^{\gamma\beta}$
Conservation of mass	$\frac{D\rho_i}{Dt} = \rho_i\sum_{j=1}^{N_i}\frac{m_j}{\rho_j}\left(v_i^{\beta} - v_j^{\beta}\right)\frac{\partial W_{ij}}{\partial x_i^{\beta}}$
Conservation of momentum	$\frac{Dv_i{}^{\alpha}}{Dt} = \sum_{j=1}^{N_i} m_j\left(\frac{\sigma_i{}^{\alpha\beta}}{\rho_i{}^2} + \frac{\sigma_j{}^{\alpha\beta}}{\rho_j{}^2}\right)\frac{\partial W_{ij}}{\partial x_i{}^{\beta}}$
Conservation of energy	$\frac{dT_i}{dt} = \frac{1}{\rho_i C_{p_i}}\sum_{j=1}^{N_i}\frac{m_j}{\rho_j}\frac{(4k_ik_j)}{(k_i+k_j)}\frac{(T_i-T_j)}{\lvert x_{ij}\rvert^2}x_{ij}\frac{\partial W_{ij}}{\partial x_i{}^{\beta}} + \dot{q}_i$
Stress decomposition	$\sigma_i{}^{\alpha\beta} = S_i{}^{\alpha\beta} - p_i\delta^{\alpha\beta}$

Table 4 Fraser–Kiss–St-Georges flow stress model constants

FKS constants	
A_1	503E6
A_2	5.0E6
A_3	70
B_1	11.99
B_2	5.611
B_3	0.1
C_1	12.8
C_2	0.01025

Table 5 Smooth particle hydrodynamic simulations constants

SPH constants	
SPH shift	0.01
$XSPH_{FRAC}$	0.01
CFL	0.5
Time scaling	50
Av_1	0.38
Av_2	0.002
Search frequency	5
SPH shift	0.01

Table 6 Phase-field and Kocks–Mecking simulation constants

Phase field and KM parameters	
α	0.5
A1	2.56×10^{44}
A2	8.17
b	2.58×10^{-8}
c	1.82×10^{13}
d	1
G	2.69×10^{8}
k_1	4.27×10^{8}
M_0	0.81
Q_a	1.45×10^{5}
Q_b	89,375
δ	1.2
γ	0.214
ρ_c	5.51×10^{13}
R	8.314
dt	10^{-5}
T	329.14

Acknowledgements Distribution Statement A: Approved for public release. Distribution is unlimited. A portion of this work was supported by the US Department of Defense Strategic Environmental Research and Development Program WP21-C4–1102. The authors would like to thank Dr. Dustin Avery for his help with Figure 1.

Declarations

Conflict of interest On behalf of all authors, the corresponding author states that there is no conflict of interest.

References

1. Avery DZ et al (2018) Fatigue behavior of solid-state additive manufactured inconel 625. JOM 70(11):2475–2484. https://doi.org/10.1007/s11837-018-3114-7
2. Beck SC et al (2023) Examination of microstructure and mechanical properties of direct additive recycling for Al–Mg–Mn alloy machine chip waste. Mater Des 228:111733. https://doi.org/10.1016/j.matdes.2023.111733
3. Phillips BJ et al (2019) Microstructure-deformation relationship of additive friction stir-deposition Al–Mg–Si. Materialia 7:100387. https://doi.org/10.1016/j.mtla.2019.100387
4. Opprecht M, Garandet J-P, Roux G, Flament C, Soulier M (2020) A solution to the hot cracking problem for aluminium alloys manufactured by laser beam melting. Acta Mater 197:40–53. https://doi.org/10.1016/j.actamat.2020.07.015
5. Yu H, Mishra R (2021) Additive friction stir deposition: a deformation processing route to metal additive manufacturing. Mater Res Lett 9:71–83. https://doi.org/10.1080/21663831.2020.1847211
6. Yu H, Xin Y, Wang M, Liu Q (2018) Hall-Petch relationship in Mg alloys: a review. J Mater Sci Technol 34(2):248–256. https://doi.org/10.1016/j.jmst.2017.07.022
7. Lin Y-J, Lin C-S (2021) Galvanic corrosion behavior of friction stir welded AZ31B magnesium alloy and 6N01 aluminum alloy dissimilar joints. Corros Sci 180:109203. https://doi.org/10.1016/j.corsci.2020.109203
8. Lee J-H, Lee C-M, Kim D-H (2022) Repair of damaged parts using wire arc additive manufacturing in machine tools. J Mater Res Technol 16:13–24. https://doi.org/10.1016/j.jmrt.2021.11.156
9. Pyles R (2003) Aging aircraft: USAF workload and material consumption life cycle patterns. Santa Monica, Rand, CA
10. Kincaid KC, MacPhee DW, Stubblefield GG, Jordon JB, Rushing TW, Allison PG (2023) A finite volume framework for the simulation of additive friction stir deposition. J Eng Mater Technol 145:031002. https://doi.org/10.1115/1.4056642
11. Stubblefield GG, Fraser K, Phillips BJ, Jordon JB, Allison PG (2021) A meshfree computational framework for the numerical simulation of the solid-state additive manufacturing process, additive friction stir-deposition (AFS-D). Mater Des 202:109514. https://doi.org/10.1016/j.matdes.2021.109514
12. Fraser K, St-Georges L, Kiss LI (2023) A mesh-free solid-mechanics approach for simulating the friction stir-welding process | IntechOpen. https://doi.org/10.5772/64159 Accessed 25 Jul 2023
13. Li L, Gupta V, Li X, Reynolds AP, Grant G, Soulami A (2022) Meshfree simulation and experimental validation of extreme thermomechanical conditions in friction stir extrusion. Comput Part Mech 9(4):789–809. https://doi.org/10.1007/s40571-021-00445-7
14. Profizi P, Combescure A, Ogawa K (2016) SPH modeling of adhesion in fast dynamics: application to the cold spray process. Comptes Rendus Mécanique 344(4):211–224. https://doi.org/10.1016/j.crme.2016.02.001
15. Holm EA, Battaile CC (2001) The computer simulation of microstructural evolution. JOM 53(9):20–23. https://doi.org/10.1007/s11837-001-0063-2
16. Wolfram S (1983) Statistical mechanics of cellular automata. Rev Mod Phys 55(3):601–644. https://doi.org/10.1103/RevModPhys.55.601
17. Chen L-Q (2002) Phase-field models for microstructure evolution. Ann Rev Mater Res 32(1):113–140. https://doi.org/10.1146/annurev.matsci.32.112001.132041
18. Fan D, Chen L-Q (1997) Computer simulation of grain growth using a continuum field model. Acta Mater 45(2):611–622. https://doi.org/10.1016/S1359-6454(96)00200-5
19. Chen L et al (2015) An integrated fast Fourier transform-based phase-field and crystal plasticity approach to model recrystallization of three dimensional polycrystals. Comput Methods Appl Mech Eng 285:829–848. https://doi.org/10.1016/j.cma.2014.12.007
20. Documentation—Thermo-Calc manuals and help, Thermo-Calc Software. https://thermocalc.com/support/documentation/ Accessed 25 Jul 2023
21. Gorsse S, Chen Y-T, Hsu W-C, Murakami H, Yeh A-C (2021) Modeling the precipitation processes and the formation of hierarchical microstructures in a single crystal high entropy superalloy. Scr Mater 193:147–152. https://doi.org/10.1016/j.scriptamat.2020.11.002
22. McDowell DL (1997) Multiaxial small fatigue crack growth in metals. Int J Fatigue 19(93):127–135. https://doi.org/10.1016/S0142-1123(97)00014-5
23. Jordon JB, Gibson JB, Horstemeyer MF, Kadiri HE, Baird JC, Luo AA (2011) Effect of twinning, slip, and inclusions on the fatigue anisotropy of extrusion-textured AZ61 magnesium alloy. Mater Sci Eng A 528(22):6860–6871. https://doi.org/10.1016/j.msea.2011.05.047
24. Avery DZ et al (2020) Influence of grain refinement and microstructure on fatigue behavior for solid-state additively manufactured Al–Zn–Mg–Cu Alloy. Metall Mater Trans A 51(6):2778–2795. https://doi.org/10.1007/s11661-020-05746-9
25. Yang X, Liu M, Peng S (2014) Smoothed particle hydrodynamics modeling of viscous liquid drop without tensile instability. Comput Fluids 92:199–208. https://doi.org/10.1016/j.compfluid.2014.01.002
26. Fraser K (2017) Robust and efficient meshfree solid thermomechanics simulation of friction stir welding. https://doi.org/10.13140/RG.2.2.13318.68169
27. Stubblefield GG et al (2022) Elucidating the influence of temperature and strain rate on the mechanics of AFS-D through a combined experimental and computational approach. J Mater Process Technol 305:117593. https://doi.org/10.1016/j.jmatprotec.2022.117593
28. Takaki T, Hisakuni Y, Hirouchi T, Yamanaka A, Tomita Y (2009) Multi-phase-field simulations for dynamic recrystallization. Comput Mater Sci 45:881–888
29. Humphreys FJ, Hatherly M (2004) Chapter 13—hot deformation and dynamic restoration. In: Humphreys FJ, Hatherly M (eds) Recrystallization and related annealing phenomena, 2nd edn.

Elsevier, Oxford, pp 415–V. https://doi.org/10.1016/B978-008044164-1/50017-7
30. Kocks UF (1976) Laws for work-hardening and low-temperature creep. J Eng Mater Technol 98(1):76–85. https://doi.org/10.1115/1.3443340
31. Bailey JE, Hirsch PB (1960) The dislocation distribution, flow stress, and stored energy in cold-worked polycrystalline silver. Philos Mag J Theor Exp Appl Phys 5(53):485–497. https://doi.org/10.1080/14786436008238300
32. Miura H, Ozama M, Mogawa R, Sakai T (2003) Strain-rate effect on dynamic recrystallization at grain boundary in Cu alloy bicrystal. Scr Mater 48(10):1501–1505. https://doi.org/10.1016/S1359-6462(03)00053-8
33. Roberts W, Ahlblom B (1978) A nucleation criterion for dynamic recrystallization during hot working. Acta Metall 26(5):801–813. https://doi.org/10.1016/0001-6160(78)90030-5
34. Zhang Y, Sills RB (2023) Strengthening via orowan looping of misfitting plate-like precipitates. J Mech Phys Solids 173:105234. https://doi.org/10.1016/j.jmps.2023.105234
35. Rokni MR, Widener CA, Champagne VK, Crawford GA (2015) Microstructure and mechanical properties of cold sprayed 7075 deposition during non-isothermal annealing. Surf Coat Technol 276:305–315. https://doi.org/10.1016/j.surfcoat.2015.07.016
36. MacKenzie DS (2016) Metallurgy of heat treatable aluminum alloys. In: Heat treat nonferr alloys; ASM International, Materials Park, USA. https://doi.org/10.31399/asm.hb.v04e.a0006287
37. Kelly PM (1972) The effect of particle shape on dispersion hardening. Scr Metall 6(8):647–656. https://doi.org/10.1016/0036-9748(72)90120-2
38. Dixit M, Mishra RS, Sankaran KK (2008) Structure–property correlations in Al 7050 and Al 7055 high-strength aluminum alloys. Mater Sci Eng A 478(1):163–172. https://doi.org/10.1016/j.msea.2007.05.116
39. Embury JD, Lloyd DJ, Ramachandran TR (1989) 22—strengthening mechanisms in aluminum alloys. In: Vasudevan AK, Doherty RD (eds) Treatise on materials science and technology in aluminum alloys—contemporary research and applications, vol 31. Elsevier, London, pp 579–601
40. Shercliff HR, Ashby MF (1990) A process model for age hardening of aluminium alloys—I: the model. Acta Metall Mater 38(10):1789–1802. https://doi.org/10.1016/0956-7151(90)90291-N
41. Crystals | Free full-text | Stable stacking faults bounded by Frank Partial dislocations in Al7075 formed through precipitate and dislocation interactions. https://www.mdpi.com/2073-4352/7/12/375 Accessed 25 Jul 2023
42. Ardell AJ (1985) Precipitation hardening. Metall Trans A 16(12):2131–2165. https://doi.org/10.1007/BF02670416
43. Smallman RE (2016) Modern physical metallurgy. Elsevier
44. Ungär T, Lendvai J, Kovács I, Groma G, Kovács-Csetényi E (1976) Quantitative investigation of the reversion process of GP zones in an Al–Zn–Mg Alloy. Int J Mater Res 67(10):683–687. https://doi.org/10.1515/ijmr-1976-671006
45. Dieter PGE (1988) Mechanical metallurgy. 3rd ed., Mc Graw-Hill Book Co., New York 1986. XXIII + 751 p., DM 138.50, ISBN 0–07–016893–8. Cryst Res Technol 23(2):194–194. https://doi.org/10.1002/crat.2170230211
46. Avery DZ et al (2022) Evaluation of microstructure and mechanical properties of Al–Zn–Mg–Cu alloy repaired via additive friction stir deposition. J Eng Mater Technol 144:031003. https://doi.org/10.1115/1.4052816
47. Wang L, Yang X, Robson JD, Sanders RE, Liu Q (2020) Microstructural evolution of cold-rolled AA7075 sheet during solution treatment. Materials 13(12):2734. https://doi.org/10.3390/ma13122734
48. Fan Y, Tang X, Wang S, Chen B (2021) Comparisons of age hardening and precipitation behavior in 7075 alloy under single and double-stage aging treatments. Met Mater Int 27(10):4204–4215. https://doi.org/10.1007/s12540-020-00875-7
49. Mehri A, Abdollah-zadeh A, Entesari S, Saeid T, Wang JT (2023) The effects of friction stir welding on microstructure and formability of 7075–T6 sheet. Results Eng 18:101041. https://doi.org/10.1016/j.rineng.2023.101041